



Extraction of wind and temperature information from hybrid 4D-Var assimilation of stratospheric ozone using NAVGEM

Douglas R. Allen, Karl W. Hoppel, David D. Kuhl

Remote Sensing Division, Naval Research Laboratory, Washington, DC, USA

5 *Correspondence to:* D. R. Allen (douglas.allen@nrl.navy.mil)



Abstract.

Extraction of wind and temperature information from stratospheric ozone assimilation is examined within the context of the Navy Global Environmental Model (NAVGEM) hybrid 4D-Var data assimilation (DA) system. Ozone can improve the winds and temperatures through the two different DA mechanisms. First, through the “flow-of-the-day” ensemble background error covariances that are blended together with the static background error covariance. Second, via the ozone continuity equation in the tangent linear model and adjoint used for minimizing the cost function. All experiments assimilate actual conventional data and satellite-derived wind vectors in order to maintain nearly the same realistic troposphere. In the stratosphere, the experiments assimilate simulated ozone and/or radiance observations in various combinations. The simulated observations are taken from a 16-day truth experiment (TE), which is an analysis with no stratospheric observations. The impact of ozone on the analysis is evaluated by comparing the experiments to the TE. Ozone assimilation is found to benefit the winds and temperatures when data are of sufficient quality and frequency. For example, global hourly ozone data with no error constrains the stratospheric winds and temperature to within $\sim 2 \text{ ms}^{-1}$ and $\sim 1 \text{ K}$, respectively. This demonstrates that there is dynamical information in the ozone distribution that can potentially be used to improve the stratosphere. This is particularly important for the tropics, where radiance observations have difficulty constraining winds due to their broad weighting functions and breakdown of geostrophic balance. Global ozone assimilation provides the largest benefit when the hybrid blending coefficient is an intermediate value (0.5 was used in this study), rather than 0.0 (no ensemble background error covariances) or 1.0 (no static background error covariances), which is consistent with other hybrid DA studies. Reduction of the ozone sampling frequency, addition of observational noise, or inclusion of radiance observations all reduce the benefit of ozone. For example, a single polar-orbiting ozone measurement set with realistic errors has no significant impact on the wind analysis when a full suite of radiance observations is also assimilated. An examination of cross-correlations between ozone and other variables shows that a single ozone observation behaves like a potential vorticity (PV) “charge”, or a monopole of PV, with rotation about a vertical axis and vertically oriented temperature dipole. Further understanding of this relationship may help in designing observation systems that would optimize the impact of ozone on the dynamics.

1 Introduction

The spatial-temporal variability of long-lived tracers such as stratospheric ozone contains dynamical information that can potentially be exploited to improve analyses of winds and temperature in the stratosphere and mesosphere, where direct wind observations are largely absent. Theoretical studies have examined tracer-wind interactions within a variety of data assimilation (DA) systems including extended Kalman Filter (EKF) (Daley, 1995, 1996), 4D Variational assimilation (4D-Var) (Riishøjgaard, 1996; Peuch et al., 2000; Andersson et al., 2007; Peubey and McNally, 2009; Semane et al., 2009; Han and McNally, 2010; Dragani and McNally, 2013; Allen et al., 2013, 2014), Ensemble Kalman Filter (EnKF) (Milewski and Bourqui, 2011, Allen et al., 2015), and hybrid 4D-Var (Allen et al., 2016). While these studies show that strong potential exists for wind extraction from tracer assimilation, the operational benefit has yet to be obtained. This study attempts to move one



step further toward determining whether ozone assimilation can benefit winds and temperatures in operational numerical weather prediction (NWP) models, focusing on ozone-dynamical (i.e., wind and temperature) interactions within a hybrid 4D-Var system, the Navy Global Environmental Model (NAVGEM), at a reduced operational model resolution but with conventional (non-radiance) operational observational data along with simulated radiance and ozone observations based on a truth experiment.

There are two primary ways that ozone can influence winds in hybrid 4D-Var DA. The first way is via the ensemble cross-correlations between ozone and other variables that are blended into the initial background error covariance. These so-called “errors of the day” allow ozone to influence dynamical variables directly. Allen et al. (2014, 2015), in shallow water model studies, showed that including these cross-correlations provides additional ozone-wind benefit over conventional 4D-Var that excludes initial cross-covariances between ozone and other variables. Second, if ozone is included in the cost function, increments to the dynamical fields at the beginning of the analysis window (i.e., strong-constraint 4D-Var), will perturb the difference between the linearized ozone forecast and the ozone observations distributed throughout the analysis time window. This linear approximation and adjoint of the tracer continuity equation propagate the ozone sensitivities over the analysis time window (see Allen et al. (2013) for a 1-D heuristic analytical solution to this problem to illustrate ozone influence in 4D-Var). Thereby ozone observations can influence the winds indirectly as the system attempts to reduce the ozone innovations via both wind and ozone increments. Note that a third way that ozone assimilation could potentially benefit winds is that improved ozone fields could result in improved radiative calculations in the forecast model; we do not attempt to address this mechanism in the current study.

The overall goal of this work is to evaluate how ozone interacts with winds and temperatures in a full NWP system (described in Sect. 2). We first examine the characteristics of the ensemble cross-covariances in order to understand how ozone and other variables relate (Sect. 3). We next look at how well ozone by itself can constrain the stratospheric dynamics (Sect. 4). The last part of the paper (Sect. 5) examines ozone assimilation in the presence of simulated radiance observations in order to determine whether ozone can provide added value. Sect. 6 provides a summary and conclusions.

2. Model description

2.1 Forecast model

This study uses a reduced resolution version of the operational NAVGEM described in Hogan et al. (2014). The NAVGEM global forecast model uses a semi-Lagrangian/semi-implicit integration of the hydrostatic equation, the first law of thermodynamics, and conservation of moisture and ozone. This study uses a 60 level hybrid sigma-pressure coordinate (top at 0.05 hPa) as described in Eckermann et al. (2009). The model is run at a relatively low resolution of T47 (144 longitudes \times 72



latitudes, for a Gaussian grid spacing of $\sim 2.5^\circ$ at the Equator). The model time step is 1800 s. The same forecast configuration and resolution are used for the control (outer loop) and the ensemble forecasts (inner loop).

2.2 Hybrid 4D-Var data assimilation system

NAVGEM employs a hybrid 4D-Var method, which is becoming increasingly popular at operational NWP centers (e.g., Buehner et al., 2010; Bonavita et al., 2012; Clayton et al., 2013; Kuhl et al., 2013; Kleist and Ide, 2015). NAVGEM minimizes a quadratic cost function using the accelerated representer approach as described in Xu et al. (2005) and Rosmond and Xu (2006). The conventional initial background error covariance $\mathbf{B}_0^{\text{con}}$ is calculated using an analytic formulation that employs the hydrostatic relationship in the vertical between geopotential and temperature, and wind-geopotential correlations based on approximate geostrophic balance on an f -plane, i.e., constant Coriolis parameter with latitude (Daley, 1991; Daley and Barker, 2001; Kuhl et al., 2013). There is no coupling between ozone and dynamical variables in $\mathbf{B}_0^{\text{con}}$, but coupling between these variables does develop implicitly over the 4D-Var time window. The only difference between the hybrid 4D-Var used in this study and Kuhl et al. (2013) is the incorporation of ozone observations in the analysis and ozone in the ensemble forecasts and forecast error covariance.

The tangent linear model (TLM) currently used in NAVGEM is based on linearization of the Navy Operational Global Atmospheric Prediction System (NOGAPS) global spectral forecast model (Hogan et al., 1991). Relevant details of the TLM and adjoint (ADJ) used in this study are provided in Rosmond (1997). The TLM and ADJ are also run at T47 resolution with 60 vertical levels, as is the nonlinear forecast model, but with a reduced time step of 900 s. The TLM has parameterizations for surface flux and vertical mixing based on Louis (1979), but does not include any other physical parameterizations such as radiation, ozone chemistry, and gravity wave drag. The 4D-Var system runs with a 6-hour analysis window, and the analysis at the middle of one window is used to initialize a 9-hour forecast that serves as the background for the next update cycle.

The ensemble consists of 80 members, which are updated each cycle using the ensemble transform (ET) approach described by McLay et al. (2008, 2010) and Kuhl et al. (2013). The ET scheme transforms the previous 6-h ensemble perturbations into a new set of initial perturbations such that the initial ensemble covariance is consistent with a prescribed estimate of the analysis error variance. The ensemble covariance, $\mathbf{B}_0^{\text{ens}} = \mathbf{X}\mathbf{X}'^T / (N_{\text{ens}} - 1)$, is calculated at the start of each 6-hour window using the ensemble states \mathbf{X}' ; the prime indicates perturbation from the ensemble mean, the superscript T indicates transpose, and N_{ens} is the ensemble size. The ensemble covariance is then blended together with $\mathbf{B}_0^{\text{con}}$ using $\mathbf{B}_0^{\text{hybrid}} = (1 - \alpha)\mathbf{B}_0^{\text{con}} + \alpha\mathbf{S} \circ \mathbf{B}_0^{\text{ens}}$, where α is a blending coefficient between 0 and 1, \mathbf{S} is the localization function, and the open circle indicates the Schur product. The horizontal localization is based on a second-order autoregressive function and



the vertical localization employs a Gaussian log-sigma correlation as described in Daley and Barker (2001) and Kuhl et al. (2013). The ensemble was initialized using NAVGEM analyses from a separate experiment that included conventional data along with radiances and Microwave Limb Sounder ozone and temperature. This experiment was run at T119 with 74 levels and was downsampled to the T47L60 resolution used for this study. The data were sampled at 18 Z on 80 consecutive days, starting 2 May 2014. Initial ensemble standard deviations are presented in Sect. 3.1.

2.3 Observations

The experiments in this study assimilate both actual observations (in the troposphere) and simulated observations computed from the truth experiment (described in Sect. 2.4). The tropospheric observations include a standard suite of operational measurements, including surface observations from ships, buoys, and land surface stations, upper air observations from radiosondes and aircraft, and satellite-derived winds (Global Positioning System (GPS) observations are not included for this particular study). The standard NAVGEM operational data quality control and thinning algorithms are used, and the resulting tropospheric observation counts range from ~750,000 to 1,000,000 observations for each 6-h cycle.

For the simulated ozone observations, three different sampling patterns are used: global, polar-orbiting, and random (See Fig. 1). The global observations are an approximately equal-area sampling, generated by subdividing an icosahedral base into a triangular grid with ~300 km spacing (3840 elements). To avoid both horizontal and vertical interpolation by the DA, the ozone observation locations were moved to the nearest model grid points and the ozone was sampled vertically on the model levels. Seventeen vertical levels in the stratosphere are used, ranging from 78 to 1.2 hPa (~20 to 50 km altitude). The temporal sampling for the global observations is 1 h, matching the forecast output sampling. For the assimilation of these observations, the observation error covariance is uncorrelated with a specified standard deviation σ_{ob} . We will examine cases with perfect observations (i.e., no random error added) and cases with the applied random error. Note that for the perfect observations, we do not set σ_{ob} exactly to zero, but to a reasonably small value of 0.1 ppmv. Setting σ_{ob} to zero causes the cost function to become singular and prevents the solution from converging. The second set of ozone observations simulates a polar-orbiting limb sounder, and was created by sampling the TE at the observation locations of the Aura Microwave Limb Sounder (MLS) instrument. There are approximately 3500 observations per day for MLS, along a flight track shown in Fig. 1b. For the polar-orbiting data we also move the locations to the nearest model grid point and sample vertically on the same model levels. The third set of ozone observations, which we call “random,” sub-samples the global observations randomly in space and time at a frequency of 3500 per day, which is a similar frequency to that of the polar-orbiting observations. This provides a test of whether spreading the information from polar-orbiting sampling would make the data more useful for extracting wind and temperature information.

Some of the experiments assimilate simulated stratospheric radiance observations, in order to assess the value of ozone in combination with a typical set of radiance observations. NAVGEM routinely assimilates microwave and infrared radiances



from a number of sounders. In this study, simulated radiances are created using actual data sampling from Advanced-Microwave Sounding Unit (AMSU-A), Atmospheric Infrared Sounder (AIRS), Advanced Technology Microwave Limb Sounder (ATMS), and Infrared Atmospheric Sounding Interferometer (IASI) (see Fig. 2 for an example of radiance observations for one update cycle). During the creation of the truth experiment, actual radiance observations are processed to the point where background radiance values are calculated, but are then omitted from the DA solver. The background radiance values then become “perfect” simulated radiances. Because the simulated radiances are created and then assimilated using same radiative transfer model, they are unbiased “perfect model” data. For the radiance and ozone assimilation experiments (Sect. 5), we add Gaussian random noise to the perfect data, matching the observation error values used in NAVGEM for the actual instruments. The variational radiance bias correction scheme in the DA is disabled for the simulated radiances. This is a best-case scenario for the radiances, since the DA of true radiances always includes biases. Addressing the impact of bias correction in the context of ozone assimilation is beyond the scope of this paper.

2.4 Truth experiment

The experimental design (described in more detail in Sect. 2.5) is based on a truth experiment (TE) that is used to simulate observations that are assimilated back into the system and also to evaluate all other experiments. Our goal was to examine stratospheric assimilation and analysis with a constant, realistic troposphere that is essentially independent of our experiments. This could be accomplished by creating a free-running nature forecast and then simulating a full set of conventional tropospheric observations. Instead, we took a simpler approach in which our TE is a normal cycling analysis in which only tropospheric data (pressures > 100 hPa) are assimilated. The stratospheric analysis of the TE can be viewed as a mechanistic forecast forced by a realistic troposphere, which is then used to create simulated stratospheric observations. All subsequent experiments, with differing stratospheric observations, assimilate the same set of tropospheric observations. This gives nearly identical tropospheric analyses for each experiment, but differing stratospheric analysis. This approach provides a realistic evaluation of how differing stratospheric observations impact a typical global analysis. We initialized the TE on 15 November 2014 (00Z) and ran through 1 December 2014 (00Z), for a total of 16 days with 64 cycles.

The meteorological conditions for the middle stratosphere are illustrated in Fig. 3, which shows the ozone and geopotential height at 10.5 hPa (~32 km) from 15-30 Nov 2014. The Northern Hemisphere (NH) stratospheric polar vortex, indicated by low ozone mixing ratio and enclosed height contours, is seen on 15 November centered slightly off the pole. A tongue of low-latitude air moves northward and eastward over the next few days as an Aleutian high starts to spin up, pushing the vortex off the pole. The vortex elongates and the minimum ozone mixing ratio increases, indicating some mixing of the vortex air outward. The Aleutian high is still strong on 30 November. Note that the ozone mixing ratio in the tropics decreases over the course of the TE; this is due to the initial conditions being drawn from an experiment that used different parameters in the ozone photochemical scheme.



In the Southern Hemisphere (SH), the large-scale circulation in the middle stratosphere is generally easterly in November, with accompanying high pressure and lower ozone mixing ratio. On 15 November, a low pressure cyclone between South America and Antarctica disrupts the normal easterly flow. Low latitude air with high ozone is pulled clockwise around the cyclone on 18 and 21 November. The cyclone diminishes in strength from 21-30 November, and the prevailing anticyclonic
5 flow center moves back towards the pole.

2.5 Experimental design

We perform two types of stratospheric assimilation experiments: ozone-only assimilation and ozone/radiance assimilation. To illustrate the differences between these experiments, Fig. 4 provides a schematic diagram. Both types of experiment use the same TE and observation database (note that all experiments assimilate the same tropospheric data). Except for the TE, all
10 experiments use perturbed initial conditions in the stratosphere. The perturbation is performed by using a different stratospheric analyses (at pressures less than 100 hPa) based on NAVGEM experiments that differ in terms of model resolution and data assimilated, resulting in slightly different dynamical fields. The ozone fields, however, are initially identical. Figure 5 shows the zonal mean differences between perturbed and unperturbed initial conditions for zonal wind and temperature. Large differences occur in the tropical upper stratosphere and throughout the lower mesosphere.

15 For the ozone-only assimilation (results presented in Sect. 4), a baseline experiment (BE) is performed by running the system from the perturbed initial conditions and assimilating only the tropospheric conventional observations. As will be shown below, the stratospheric winds and temperatures in this BE deviate significantly from the TE (after 16 days, zonal mean differences of up to $\sim 80 \text{ ms}^{-1}$ occur for vector wind and $\sim 25 \text{ K}$ for temperature). When experimenting with the blending coefficient ($\alpha =$
20 0.0, 0.5, and 1.0), we must run separate TE and BE cases for each value. This is because the blending coefficient affects the tropospheric assimilation, and hence changes the reference TE for each case. Changing α examines the sensitivity of the amount of ozone-wind correlation being used from the ensemble covariances. Ozone-only assimilation experiments are next performed, which examine the limit to which ozone could potentially constrain the winds without any other data present in the stratosphere. Global data are assimilated for all three values of α (Sect. 4.2), while random and polar-orbiting data are only
25 assimilated for $\alpha = 0.5$ (Sect. 4.3). In addition, to examine sensitivity to data quality, experiments are performed for $\alpha = 0.5$ with assimilation of global ozone data with imposed observational errors (Sect. 4.4).

In the ozone/radiance assimilation experiments (results presented in Sect. 5), we test the extent to which assimilating ozone data can reduce the initial errors relative to errors in a system constrained by realistic radiance observations. First, we create a
30 BE by assimilating noisy radiances created from the TE. Then experiments are performed in which either global, random, or polar-orbiting data are assimilated in addition to the radiances using either perfect ozone and ozone with imposed random errors.



3. Discussion of background errors

The background error covariance is a critical component of the hybrid 4D-Var system. Hybrid 4D-Var combines a conventional error covariance with a localized ensemble covariance in order to take advantage of both the high-rank properties of the conventional and flow-of-the-day properties of the ensemble components. In this section, we first examine the latitude/pressure cross-sections and horizontal maps of the background error standard deviations (i.e., the square root of the diagonal terms of the covariance matrix). We denote the background error standard deviations as σ_{con} , σ_{ens} , and σ_{hyb} for the conventional, ensemble, and hybrid, respectively. Next, we examine the cross-correlation terms, which indicate how errors are correlated with other variables and spatial locations. Our particular interest is the patterns that describe how ozone correlates with other variables.

3.1 Comparing conventional and ensemble error standard deviation

Figure 6 shows latitude-pressure cross-sections of σ_{con} and σ_{ens} for zonal wind, temperature, and ozone. The σ_{ens} has been zonally averaged, while σ_{con} is formulated as a zonal mean model. The conventional errors are shown for 15 November 2014 only, while the ensemble errors are provided for 15 November and 1 December 2014. The σ_{con} for zonal wind increases with altitude from $\sim 2 \text{ m s}^{-1}$ in the troposphere to $\sim 8 \text{ m s}^{-1}$ at 0.1 hPa. The σ_{ens} for zonal wind on 15 November shows more structure, with higher values in the upper troposphere and lower mesosphere, and low values in the extratropical stratosphere. As the ensemble evolves, the zonal wind σ_{ens} generally increases, particularly in the mesosphere.

The temperature σ_{con} is relatively small, ranging from ~ 0.5 to $\sim 2 \text{ K}$, with lower values in the tropics. The initial σ_{ens} for temperature has a similar geographic structure as zonal wind, with elevated values in the upper troposphere and mesosphere.

The temperature σ_{ens} generally increases over the next two weeks, with very large values occurring above $\sim 1 \text{ hPa}$. For ozone, the σ_{con} is prescribed as a constant value of 0.3 ppmv, except for elevated values in the tropical troposphere. The initial ozone σ_{ens} is elevated in the tropical middle stratosphere and SH lower and upper stratosphere. The ozone errors evolve to have three regions of enhanced σ_{ens} located in the middle stratosphere in the tropics and extratropics of each hemisphere, with relative minima in the subtropics. Lower values are seen both in the troposphere and upper stratosphere/mesosphere, which largely reflect the lower ozone mixing ratios in these levels.



3.2 Horizontal maps of ozone σ_{ens}

The ozone σ_{ens} shows strong geographic patterns that are related to the flow-of-the-day. Figure 7 shows horizontal maps of the ozone σ_{ens} for the same level (10.5 hPa) and dates as in Fig. 3. Geopotential contours are overlaid on the σ_{ens} to facilitate comparison with the flow. On 15 November, the initial σ_{ens} is not aligned with the flow, since the initial ensemble was constructed with analyses on consecutive days from an offline experiment; after 3 days, however, flow-like patterns start to emerge. On 18 November, the σ_{ens} in the NH is larger within the polar vortex and in the tropics, while smaller values occur outside of the vortex. This pattern strengthens over the next several days so that by 24 November the vortex/extra vortex distinction is prominent. The high σ_{ens} in the vortex is in a location where the ozone mixing ratio is actually low (see Fig. 3). Long streamers of high σ_{ens} are visible in the NH throughout this period, circling around the outer edges of the polar vortex and Aleutian high, where the ozone gradients are large. These patterns are significant for data assimilation, since they will affect the weight that is given to the observations. For example, in the polar vortex the σ_{ens} is large, so ozone observations in this region will have a larger impact than those outside of the vortex.

The ozone σ_{ens} in the SH also shows a rapid spin-up from an initial state that is approximately constant in the zonal direction. Swirls are seen on 18 November in the cyclonic flow, with a low σ_{ens} “tongue” surrounded by high σ_{ens} . From 18-27 November, the σ_{ens} in the anticyclonic closed height contours increases. A tongue of low σ_{ens} occurs between the two flow regimes on 24 and 27 November, apparently advected by the nearly cross-polar flow. By 30 November, the σ_{ens} pattern shows generally large values at high latitudes, small values in the tropics, and complicated structure in the extratropics. While a complete analysis of the causes of these features is beyond the scope of this paper, it is clear that the σ_{ens} is strongly flow-dependent and may (at least in the experiments with $\alpha = 1.0$) result in large differences in weighting of ozone observations; note that the errors range from -0.04 to 0.99 ppmv at 10.5 hPa for 30 November.

3.3 Ensemble ozone-wind cross-covariances

As discussed in Sect. 1, ozone can influence winds and temperatures via the ensemble background error cross-correlations. Here we show an example of these cross-correlations. Figure 8 provides a composite view of the impact of a single ozone observation at 10.5 hPa and latitude of 28.6° S. The composite was created by separately calculating the spatial correlations of ozone at 36 longitude points ($0^\circ, 10^\circ, 20^\circ, \dots, 350^\circ$) with all other points and variables. The correlations were then shifted to a common longitude of 180° E and averaged to reduce spurious noise. The top row of Fig. 8 shows the horizontal



correlations. The ozone-ozone correlation (Fig. 8a) has a maximum of 1.0 at the observation point, and then decreases gradually in each direction, with a larger decorrelation length in the zonal direction. The ozone correlates strongly with vorticity (Fig. 8b), with the ozone-vorticity correlation having a similar zonally-oriented shape. The ozone-height correlation (Fig. 8c) is more isotropic and represents an anticyclonic circulation, which is counter clockwise in the SH, as seen in the correlations with zonal (Fig. 8d) and meridional (Fig. 8e) wind. The ozone-temperature correlation (Fig. 8f) is weak at the level of the observation, but vertical cross-sections in longitude (Fig. 8l) and latitude (Fig. 8r) reveal a strong dipole pattern with cold (warm) temperatures above (below) the observation. Vorticity (Fig. 8h, n) and height (Fig. 8l, o) correlations are vertically oriented similar to the ozone-ozone correlation, with slight westward and southward tilting with height; the wind cross-sections (Fig. 8j, k, p, q) show that the anticyclonic circulation extends above and below the observation.

10

The temperature and circulation patterns revealed in the correlations of Fig. 8 are similar to those associated with the potential vorticity (PV) “charge” concept developed by Bishop and Thorpe (1994). In this analogy to electrostatics, an elementary PV charge is associated with a field that produces a circulation about the vertical axis and a vertically oriented temperature dipole (see also Fig. 14 of Allen et al., 1997). That a single ozone observation would produce the same circulation patterns as a monopole of PV makes sense, since PV and ozone are both quasi-conserved quantities and will therefore have strong correlations. The pattern is also seen at other latitudes, although its strength varies due to differing ozone gradients and geostrophic coupling. In the NH, the ozone-vorticity correlation is negative and the circulation is clockwise (anticyclonic in the NH), and the temperature dipole is similar with cold (warm) temperatures above (below) the observations. These results indicate that ozone observations can be considered as pseudo-PV observations, at least in the regions where strong ozone gradients and geostrophic balance occur; this would likely be true of other long-lived trace gases as well.

20

4. Ozone-only assimilation

Here we evaluate the influence of ozone-only assimilation on the wind and temperature (T) analyses. There are several factors that will affect the ozone-wind/T relationships in the system. The experiments focus on the sensitivity to the initial conditions, blending coefficient, sampling pattern, and observation error (see Table 1 for a complete list of experiments). To quantify the ozone impact, we calculate the root mean square (RMS) error profiles for the background and Ozone Assimilation Experiment (OAE) for vector wind and T on 1 December 2014 (00Z) in three latitude bands (NH, 30° - 90°N; TR, 30°S - 30°N; SH, 30° - 90°S). These were calculated by first computing the RMS error for zonal wind (u), meridional wind (v) and temperature (T) using the following formula (shown below for u, but similar for v and T).

25



$$u_{RMSE}^2(k) = \frac{\sum_{j=j_{\min}}^{j_{\max}} \left[\frac{1}{nlon} \sum_{i=1}^{nlon} (u(i, j, k) - u_{TE}(i, j, k))^2 \cos(lat(j)) \right]}{\sum_{j=j_{\min}}^{j_{\max}} \cos(lat(j))} \quad (1)$$

Here i , j , and k are indices for longitude (lon), latitude (lat), and vertical level, while $nlon$ indicates the number of longitudes and j_{\min} and j_{\max} indicate the latitude indices corresponding to the bounding latitudes for each region (NH, TR, or SH). To get the vector wind error, we combine the u and v errors as follows.

5

$$V_{RMSE}^2(k) = \sqrt{u_{RMSE}^2(k) + v_{RMSE}^2(k)} \quad (2)$$

4.1 Dependence on initial conditions

Before comparing the results from the various ozone assimilation experiments, we first examine the dependence on the initial conditions. If we start with zero initial error (“unperturbed”), and assimilate perfect stratospheric observations (of any type), we might expect to have zero analysis error relative to the TE. However, the inclusion of additional observations, even if they are perfect, changes the numerics of the cost function minimization (which includes all the tropospheric observations). This results in slight changes to the troposphere, which thereby forces the stratosphere away from the TE. This behavior of the system creates a limit on the level of errors we can reliably distinguish from the TE. This is illustrated in Fig. 9, which shows errors for perfect-ozone assimilation experiments started from both perturbed and unperturbed initial conditions (first 3 experiments in Table 1). The resulting vector wind and T errors after 16 days show relatively small errors in the troposphere and stratosphere (wind errors less than $\sim 2 \text{ ms}^{-1}$ in the tropics, while T errors are generally less than $\sim 1 \text{ K}$). The results with unperturbed initial conditions (black lines) show slightly smaller errors than with perturbed initial conditions (red lines), but the general profile shapes are the same. This suggests that after sufficient time, the experiments are not very sensitive to the size of the initial error.

20 4.2 Dependence on blending coefficient

The next set of experiments assimilate perfect global ozone data in the stratosphere, using blending coefficients of $\alpha = 0.0, 0.5,$ and 1.0 . For each choice of blending coefficient, three experiments are completed for the TE, BE (no ozone), and OAE (ozone). Separate TE and BE are necessary for each case, since the blending coefficient affects not only the stratosphere, but also the tropospheric analysis (see nine experiments listed for this subsection in Table 1).

25 Figure 10 shows RMS errors for the BE (dotted) and OAE (solid) for the three blending coefficients. The BE wind errors increase with altitude throughout the stratosphere, ranging from $\sim 1\text{-}2 \text{ ms}^{-1}$ at 100 hPa to $\sim 70\text{-}80 \text{ ms}^{-1}$ at 1 hPa in the NH, $\sim 25\text{-}30 \text{ ms}^{-1}$ in the tropics, and $\sim 4\text{-}5 \text{ ms}^{-1}$ in the SH. The differences in wind errors in different latitude bands reflect different



sensitivities to perturbations in the initial conditions. Due to the low sensitivity in the SH, our discussion will focus mainly on the NH and TR. The BE errors for different blending coefficients show slight differences, indicating the sensitivity of the stratosphere to changes in the DA system used for tropospheric analysis. The BE T errors are also largest in the NH and TR, with generally increasing errors with height in the stratosphere. BE T errors reach up to ~25-30 K in the NH, ~5-6 K in the TR and ~1.5-2 K in the SH.

For the OAEs, there are generally large reductions in vector wind errors throughout the stratosphere and mesosphere relative to the BE. In the NH and TR, the results with non-zero blending coefficients are better than with $\alpha = 0.0$ above about 10 hPa. This indicates that the ensemble correlations are playing a large role at higher altitudes. This is expected, since the conventional balance approximations were designed to simulate tropospheric balance conditions, and they do not take into account the influence of resolved unbalanced modes such as gravity waves. The $\alpha = 0.5$ results are slightly better than the $\alpha = 1.0$ results, suggesting that combining covariances is helpful for the system, a well-documented result in the stratosphere (e.g., Kuhl et al., 2013). The T errors for the OAEs also show reductions in the NH relative to the BE, with the $\alpha = 0.5$ producing the consistently smallest errors throughout the stratosphere and mesosphere, followed by $\alpha = 1.0$ and $\alpha = 0.0$. In the TR and SH, the $\alpha = 1.0$ results are worse than $\alpha = 0.0$ in the stratosphere.

The larger errors in $\alpha = 1.0$ may be related to spurious resolved gravity waves being generated in the system. To identify GW, Fig. 11 shows divergence patterns on 1 December 2014 at 10.5 hPa for the OAE with three blending coefficients, along with the zonal standard deviation of the divergence as a function of latitude. The divergence at this level clearly increases over the globe with more ensemble information added to the system. The globally-averaged divergence profiles are provided in Fig. 12, showing that the enhanced divergence occurs at all vertical levels. This suggests that local imbalance due to the use of localized ensemble covariance may be causing gravity waves that are propagating upward into the stratosphere and mesosphere (see Keyper, 2009 and Allen et al., 2015 for discussions of imbalance in the framework of the shallow water model and EnKF). Although more work is necessary to sort out the details, using $\alpha = 0.5$ likely provides the best results by combining reduced spurious imbalance relative to $\alpha = 1.0$ as well as enhanced flow-of-the-day information relative to $\alpha = 0.0$. We will use $\alpha = 0.5$ as the blending coefficient for the following sensitivity tests as well as for the combined ozone/radiance assimilation experiments in Sect. 5.

4.3 Dependence on sampling pattern

The previous results show that with global hourly coverage, ozone observations are able to constrain the stratospheric winds to error less than about 2 ms^{-1} and T errors less than about 1 K. This sampling is, of course, unrealistic in both horizontal and temporal coverage. Here we examine sensitivity to sampling by repeating the experiments with polar-orbiting and random sampling (see Fig. 1b,c). The polar-orbiting sampling would be similar, for example, to the MLS or Ozone Mapping and Profiler Suite (OMPS). The random sampling is not realistic, but provides a hypothetical test of what would happen if random



observations occurred with the same frequency as the polar orbiter. In each case, we assume perfect observations and σ_{ob} of 0.1 ppmv. The RMS error profiles are provided in Fig. 13.

The OAE error profiles for vector wind show that assimilation of both polar-orbiting (green) and random (red) ozone
5 observations reduce the errors relative to the BE (dotted line). Particularly in the lower stratosphere, from about 100 to 10 hPa, the wind errors remain relatively small, less than about 4 ms^{-1} . In the upper stratosphere (above 10 hPa), the errors for the polar-orbiting observations increase sharply with altitude to $\sim 50 \text{ms}^{-1}$ at 1.0 hPa. The wind errors for random sampling (red) are consistently lower than for polar-orbiting, even though both contain approximately the same number of observations. While
10 there may be some redundancy in the polar-orbiting observations due to closely spaced along-track profiles, it is also likely that the large gaps between orbit tracks (see Fig. 1b) make it difficult for the polar-orbiting observations to completely constrain the winds. While the random sampling does better than polar-orbiting, there are still rather large wind errors in the random sampling, up to $\sim 20 \text{m/s}$ in the NH and $\sim 10 \text{m/s}$ in the tropics. We note that the error reductions occur even in the mesosphere, where there are no observations, suggesting that improving the stratospheric analyses will also improve the mesosphere.

15 The OAE error profiles for T also show improvements relative to the BE when polar-orbiting observations are assimilated, with the smallest errors occurring in the lower stratosphere. However, in the NH upper stratosphere the polar-orbiting observations only constrain T to about 15 K. The experiment with random observations has smaller T errors, which are similar to the global errors in the NH and tropics up to about 10 hPa. In the SH lower stratosphere, the polar-orbiting and random cases actually have smaller T errors than the global case, and the global case has errors larger than the BE. However, the
20 magnitude of these errors are near the error limit discussed in Sect. 4. Overall, we see that the ozone-dynamical influence is strongly sensitive to the sampling pattern, but wind and T improvements are possible even with a realistic polar-orbiting satellite.

4.4 Dependence on observation error

Next, we examine the sensitivity of the analysis to the ozone observation error. First, we assimilate polar-orbiting data with
25 2% error (blue lines on Fig. 13). This is a realistic error value for the middle stratosphere; for example, Aura MLS V4.2 precision specifications are rated at 2% at 22, 10, and 5 hPa and greater than 2% elsewhere (Livesy et al., 2016). The results show slightly larger vector wind and T errors in the NH for 2% error than when perfect data were assimilated, but the errors are less than the background throughout the stratosphere and mesosphere, suggesting value added by these observations. In the tropics and SH, the 2% case is very similar to the 0% case for both vector wind and T. These results suggest that assimilating
30 actual profile measurements with realistic errors can potentially benefit the analyses.



We now add random noise to the global observations using Gaussian errors of 2%, 5%, and 10% to further examine sensitivity to errors. For each of these three cases, the specified σ_{ob} is also set to the same percent value (see Table 1). The results, in Fig. 14, show that adding noise increases the vector wind errors over the perfect observations. Below about 5 hPa, the wind errors are similar for 2%, 5%, and 10% cases, while above 5 hPa, there is generally increased error with increased observational noise. The wind errors are still relatively small even with 10% error, suggesting that the dynamic variability of ozone is large enough to allow wind information on this error level. In the SH lower stratosphere, adding ozone errors does cause errors larger than the BE case. This may be related to small variability of the ozone fields in this region.

The OAE T errors show reduction relative to the BE in the NH and TR, and errors are generally larger with more observational noise. At 10% the T errors are constrained to within ~4 K in the NH and TR and ~1.5 K in the SH. In the SH stratosphere, there is a reversal of the errors, with the 10% case showing smaller errors than the 5% or 2% cases. The cause of this reversal is uncertain, but it may be that using higher σ_{ob} in the 10% case reduces the weight of the observations and therefore results in reduced errors relative to the TE. This may become important in regions of weak tracer tendency. Allen et al. (2013) discussed this possibility in both idealized 1-D advection simulations and NAVGEM simulations of a single cycle of ozone assimilation. Overall, we conclude here that noisy observations will generally reduce the amount of wind information that can be derived from ozone, but if the σ_{ob} is specified consistent with the actual errors, then the result is generally an improvement over the no ozone baseline case. As a caveat, we remind the reader that we are only simulating random error and not biases, which could be a significant source of additional error. In the next section, we examine how ozone impacts winds and T in experiments that include realistic stratospheric radiance observations.

20 5. Ozone and radiance assimilation

5.1 Baseline experiment for radiance assimilation

In Sect. 4, we showed that ozone assimilation can benefit the winds and T in the stratosphere and mesosphere. Here, we examine the impact of ozone when the stratosphere is already constrained by radiance observations. As described in Sect. 2.3, we simulated infrared and microwave radiance observations for AMSU-A, AIRS, ATMS, and IASI for the $\alpha = 0.5$ TE case, and then added random noise. As with the ozone (Sect. 4.1), we ran experiments assimilating radiance data with both perturbed or unperturbed initial conditions. The profiles after 16 days of assimilation (not shown) were again very similar, suggesting that all the results we show are not too sensitive to initial conditions. The vector wind and T error profiles for radiance-only experiments are provided in Fig. 15. The black line shows the results for assimilation of noisy radiances. In the stratosphere, wind errors range from around 2 to 4 ms^{-1} , while T errors range from around 0.4 to 1.5 K. These are relatively small errors,



such that reducing the errors further by adding ozone assimilation is more challenging from the perspective of ozone-dynamical interactions.

Before adding ozone into the system, we also performed an experiment in which “perfect” radiances were assimilated with unperturbed initial errors. Wind and T error profiles from this case are shown in the red lines on Fig. 15. As with the assimilation of perfect ozone with unperturbed initial conditions, the experiment with perfect radiances results in errors both in the troposphere and stratosphere. As explained in Sect. 4.1, in our experimental design, inclusion of additional observations (relative to the TE), even if they are perfect, results in slight changes to the troposphere, which thereby forces the stratosphere away from the TE. Comparing Fig. 15 with Fig. 9, we see that the error profiles for perfect radiances are slightly larger than for perfect global ozone. Therefore, it is likely that radiances are the limiting factor when combining ozone and radiance data together. For this reason, we expect the errors for the combined ozone/radiance experiments to lie within black and red lines of Fig. 15 (discussed further below).

5.2 Ozone assimilation experiments

In the next set of experiments, ozone data (global, random, and polar-orbiting) are added to the noisy radiance assimilation. Figure 16 shows vertical profiles of the resulting errors for perfect ozone observation. We also include in Fig. 16 the error profiles (gray lines) from the radiance assimilation experiments shown in Fig. 15 as a comparison. Because the resulting OAE errors are very close to the radiance-only results, we also plot the error difference (OAE errors minus the black lines from Fig. 15). Positive values of this difference indicate value added due to ozone assimilation. Figure 17 shows vertical profiles of these differences for perfect ozone observations.

20

In the TR, the impact of ozone assimilation is positive for all three sampling patterns, with generally increasing impact with altitude throughout the stratosphere. Global observations reduce vector wind errors by up to $\sim 1.5 \text{ ms}^{-1}$ at the stratopause, while random and polar-orbiting data reduce tropical wind errors by about 0.5 and 0.3 ms^{-1} , respectively. In the NH and SH, global observations benefit winds throughout the stratosphere, but at a reduced amount compared with the tropics. The fact that ozone has the largest benefit in the tropics is consistent with there being less wind constraint from radiance observations. The impact of random observations in the NH and SH is positive throughout the stratosphere, but at much smaller levels ($\sim 0.1 - 0.3 \text{ ms}^{-1}$) than for global data. For polar-orbiting observations, the impact on NH and SH winds is even smaller, but still generally positive. We note that the error profiles generally lie within the perfect and noisy radiance profiles of Fig. 15, and the vector wind errors for global ozone is very close to the perfect radiance profile. This suggests that the ozone is reducing errors to near the minimum possible values, identified by the perfect radiance case.

30

Temperature error reductions show a similar pattern to the wind errors, with largest impact from the global observations in the tropical upper stratosphere, where reductions of $\sim 0.7 \text{ K}$ occur. The random and polar-orbiting observations also impact the



tropical upper stratosphere, with T error reductions of about 0.3 and 0.2 K, respectively. In the extratropics, the impact of the random and polar-orbiting observations on T is small, generally less than about 0.1 K, but generally positive. We also note that impact of ozone observations on both winds and T is generally positive in the mesosphere, above the highest observation level.

5

Next, in Figs. 18 and 19, we repeat the above comparison with 2% ozone error. The global ozone observations tend to have the largest positive impact, in the tropical middle stratosphere. However, the magnitude of the impact, for both wind errors and T errors, is much smaller than for perfect ozone. The impact of random and polar ozone observations is also smaller throughout the stratosphere. It is not surprising that the radiances overwhelm these noisy polar and random ozone observations since the total number of ozone observations (3500/4 profiles \times 17 observations/profile = 14,875) is only ~1% of the number of radiance observations (e.g., 1,768,409 observations shown in Fig. 2) for a given 6-h cycle. The very small benefit from global ozone with reasonable errors suggests that any benefit that current NWP systems gain from adding stratospheric ozone assimilation is likely not due to the dynamical ozone-wind interaction in hybrid 4D-Var.

15 These results provide a rather sobering conclusion that in the presence of realistic radiance observations, it is likely that adding ozone assimilation, from current ozone retrieval observations, will have little to no impact on the winds through the ozone-wind interactions investigated in this study. However, we add the caveat that the ozone, radiances, and model used in the study are unbiased. We did not test the effect that ozone might have when the radiances or model have bias. We also did not investigate the degradation that ozone assimilation might cause if the ozone observations are biased. Semane et al. (2009) showed a slight reduction in wind bias in the lower stratosphere when assimilating of MLS ozone data, suggesting that the ozone might help provide further benefit in the presence of model or observation biases. Further work is necessary to examine ozone impact on mean wind and temperature errors in more detail.

6. Summary and Conclusions

This study examined the potential impact of ozone assimilation on the wind and temperature analyses in the stratosphere. We used unbiased measurements and a perfect model to test the wind-dynamics interaction in hybrid 4D-Var DA, which arises from background ensemble covariances and the tracer advection in the linear/adjoint model. The structures of the ensemble cross-correlations for ozone with other variables were illustrated with a composite single ozone observation increment, formed by averaging the spatial cross-correlations for 36 points around a latitude circle. Clear patterns emerged that included rotation around a vertical axis and a vertical temperature dipole. These patterns resembled the potential vorticity “charge” concept, discussed by Bishop and Thorpe (1994). This suggests that an ozone observation, at least in the presence of sufficient spatial gradients and geostrophic balance, acts like an observation of potential vorticity. This is likely due to both quantities being



quasi-conserved in the stratosphere and therefore forming compact relationships. Further work on the understanding of these relationships may provide insight into designing ozone observing systems that would optimize the ozone-wind relationship.

Experiments were then conducted in which simulated stratospheric observations were assimilated in a cycling hybrid 4D-Var system. The resulting analyses were compared with a truth experiment that was used for simulating the observations and verifying the analyses. All experiments included a suite of conventional tropospheric observations and satellite-derived winds to constrain the troposphere. This approach allowed a controlled method for determining ozone impact on the stratospheric dynamics, while maintaining a realistic troposphere. Experiments assimilated combinations of stratospheric ozone and radiances. The mechanisms through which ozone can impact the winds in hybrid 4D-Var include both the application of cross-covariances of ozone with other fields in the initial blended background error covariance and the use of the ozone continuity equation in the tangent linear model/adjoint. We showed that using a blending coefficient of 0.5 provided better results than either 0.0 or 1.0. This is likely due the combined positive effects of the ensemble flow-of-the-day information with the negative aspects of spurious unbalanced modes spawned by the localized ensemble covariance. These aspects were discussed in the shallow water model context in Allen et al. (2016), where it was shown that the optimal blending coefficient also depends both on the data being assimilated and on the ensemble size.

Ozone assimilation clearly can benefit the winds and temperatures if sufficient high-quality observations are available. For example, global hourly ozone data with no error constrained the stratosphere to within a few ms^{-1} for the winds and ~ 1 K for temperature. This demonstrates that there is dynamical information embedded in the ozone field that could potentially be “mined” to obtain stratospheric wind and temperature information. This is particularly important for the tropics, where radiances alone have difficulty due to their large weighting functions and breakdown of geostrophic balance. Reduction of the sampling frequency and/or addition of observational noise reduced the benefit of ozone. Without radiance assimilation, ozone improved winds and temperatures, even for a single polar-orbiting measurement with realistic error. When added to simulated radiance assimilation, ozone had a very small benefit, to the extent that realistic 2% ozone error resulted in insignificant wind and temperature changes using our methodology.

In this study, we only simulated ozone vertical profile measurements, since we expect that vertical resolution is essential for the ozone-wind relationship to be robust. However, vertical sounders such as Ozone Monitoring Instrument (OMI) or OMPS could provide supplementary information to constrain the winds, particularly in the lower stratosphere (see, for example, the study by Peuch et al., 2000). Certain radiance channels also have ozone sensitivity that could potentially be exploited (Dragani and McNally, 2013). We also limited the study to unbiased ozone and radiance observations. Further work is necessary to determine the impact of ozone assimilation in a system with model and/or observation biases. Other approaches to the ozone-dynamical impact could include assimilation of radiances channels that are sensitive to ozone as well as assimilation of ozone radiances directly into the system rather than retrieved profiles. In addition, the impact of assimilation of other tracers could



be tested in a similar framework. Allen et al. (2014), in a shallow water model study, showed that nitrous oxide and water vapor could also potentially benefit winds in 4D-Var DA.

Acknowledgments

This work was funded by the U. S. Office of Naval Research. Douglas R. Allen and Karl W. Hoppel acknowledge support from Office of Naval Research base funding via Task BE-033-02-42. David D. Kuhl and Karl W. Hoppel acknowledge support from Office of Naval Research base funding via Task BE-435-050.

References

- Allen, D. R., Stanford, J. L., Elson, L. S., Fishbein, E. F., Froidevaux, L., and Waters, J. W.: The 4-day wave as observed from the Upper Atmosphere Research Satellite Microwave Limb Sounder, *J. Atmos. Sci.*, 54, 420-434, 1997,
- 10 Allen, D. R., Hoppel, K. W., Nedoluha, G. E., Kuhl, D. D., Baker, N. L., Xu, L., and Rosmond, T. E.: Limitations of wind extraction from 4D-Var assimilation of ozone, *Atmos. Chem. Phys.*, 13, 3501-3515, doi:10.5194/acp-13-3501-2013, 2013.
- Allen, D. R., Hoppel, K. W., and Kuhl, D. D.: Wind extraction potential from 4D-Var assimilation of stratospheric O₃, N₂O, and H₂O using a global shallow water model, *Atmos. Chem. Phys.*, 14, 3347-3360, doi:10.5194/acp-14-3347-2014, 2014.
- Allen, D. R., Hoppel, K. W., and Kuhl, D. D.: Wind extraction potential from ensemble Kalman filter assimilation of stratospheric ozone using a global shallow water model, *Atmos. Chem. Phys.*, 15, 5835-5850, doi:10.5194/acp-15-5835-2015, 2015.
- 15 Allen, D. R., Hoppel, K. W., and Kuhl, D. D.: Hybrid ensemble 4DVar assimilation of stratospheric ozone using a global shallow water model, *Atmos. Chem. Phys.*, 16, 8193-8204, doi:10.5194/acp-16-8193-2016, 2016.
- Andersson, E., E. Hólm, P. Bauer, A. Beljaars, G. A. Kelly, A. P. McNally, A. J. Simmons, J.-N. Thépaut, and Tompkins, A. M.: Analysis and forecast impact of the main humidity observing systems, *Q. J. Roy. Meteor. Soc.*, 133, 1473-1485, doi:10.1002/qj.1112, 2007.
- 20 Bonavita, M., Isaksen, L., and Hólm, E., 'On the use of EDA background error variances in the ECMWF 4D-Var,' ECMWF Tech Memo 664. Available at <http://old.ecmwf.int/publications/library/do/references/show?id=90381> (last access: 21 April 2015), 2012.
- 25 Bishop, C. H., and Thorpe, A. J.: Potential vorticity and the electrostatics analogy: Quasi-geostrophic theory, *Q. J. Roy. Meteorol. Soc.*, 120, 713-731, 1994.



- Buehner, M., Houtekamer, P. L., Charette, C., Mitchell, H. L., and He, B.: Intercomparison of variational data assimilation and the ensemble Kalman filter for global deterministic NWP. Part II: One-month experiments with real observations, *Mon. Wea. Rev.*, 138, 1567-1586, doi:10.1175/2009MWR3158.1, 2010.
- Clayton, A. M., Lorenc, A. C., and Barker, D. M.: Operational implementation of a hybrid ensemble/4D-Var global data
5 assimilation system at the Met Office, *Q. J. R. Meteorol. Soc.*, 139, 1445–1461. doi:10.1002/qj.2054, 2013.
- Daley, R., *Atmospheric Data Analysis*, Cambridge University Press, Cambridge, pp 150-185, 1991.
- Daley, R.: Estimating the wind-field from chemical-constituent observations - experiments with a one-dimensional extended Kalman filter, *Mon. Wea. Rev.*, 123, 181-198, doi: 10.1175/1520-0493(1995)123<0181:ETWFFC>2.0.CO;2, 1995.
- Daley, R.: Recovery of the one and two dimensional windfields from chemical constituent observations using the constituent
10 transport equation and an extended Kalman filter, *Meteorol. Atmos. Phys.*, 60, 119-136, 1996.
- Daley, R., and Barker, E.: NAVDAS Source Book 2001, NRL Publication NRL/PU/7530—01-441, available at <http://www.dtic.mil/docs/citations/ADA396883>, last access: 16 August 2017, Naval Research Laboratory, Monterey, California, USA, 163pp, 2001.
- Dragani, R., and McNally, A. P.: Operational assimilation of ozone-sensitive infrared radiances at ECMWF, *Q. J. Roy. Meteor.*
15 *Soc.*, 139, 2068-2080, doi:10.1002/qj.2106, 2013.
- Eckermann, S. D., Hoppel, K. W., Coy, L., McCormack, J. P., Siskind, D. E., Nielsen, K., Kochenash, A., Stevens, M. H., Englert, C. R., Singer, W., and Hervig, M.: High-altitude data assimilation system for the northern summer mesosphere season, *J. Atm. Sol.-Terr. Phys.*, 71, doi: 10.1016/j.jastp.2008.09.036, 531-551, 2009
- Han, W., and McNally, A. P.: The 4D-Var assimilation of ozone-sensitive infrared radiances measured by IASI, *Q. J. Roy.*
20 *Meteor. Soc.*, 136, 2025-2037, doi:10.1002/qj.708, 2010.
- Hogan, T. F., and Rosmond, T. E.: The description of the Navy Global Operational Prediction System's spectral forecast model, *Mon. Wea. Rev.*, 119, 1786-1815, 1991.
- Hogan, T., Liu, M., Ridout, J., Peng, M., Whitcomb, T., Ruston, B., Reynolds, C., Eckermann, S., Moskaitis, J., Baker, N., McCormack, J., Viner, K., McLay, J., Flatau, M., Xu, L., Chen, C., Chang, S.: The Navy Global Environmental Model.
25 *Oceanography* 27, 116–125, 2014.
- Kepert, J. D.: Covariance localisation and balance in an ensemble Kalman filter, *Q. J. Roy. Meteor. Soc.*, 135, 1157-1176, doi:10.1002/qj.443, 2009.
- Kleist, D. T., and Ide, K.: An OSSE-based evaluation of hybrid variational-ensemble data assimilation for the NCEP GFS. Part II: 4D-EnVar and hybrid variants, *Mon. Wea. Rev.*, 143, 452-470, doi:10.1175/MWR-D-13-00350.1, 2015.

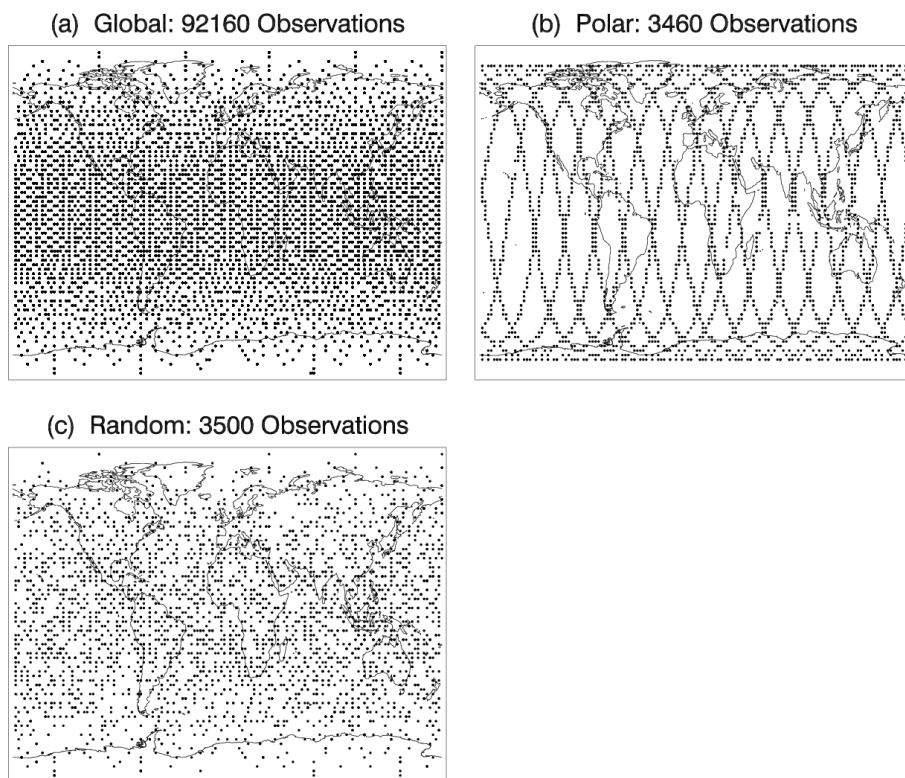


- Kuhl, D. D., Rosmond, T. E., Bishop, C. H., McLay, J., and Baker, N. L.: Comparison of Hybrid Ensemble/4DVar and 4DVar within the NAVDAS-AR data assimilation framework, *Mon. Wea. Rev.*, 141, 2740-2758, doi:10.1175/MWR-D-12-00182.1, 2013.
- Livesy, N. J., Read, W. G., Wagner, P. A., Froidevaux, L., Lambert, A., Manney, G. L., Millan Valle, L. F., Pumphrey, H. C., Santee, M. L., Schwartz, M. J., Wang, S., Fuller, R. A., Jarnot, R. F., Knosp, B. W., Martinez, E.: Version 4.2x Level 2 data quality and description document, Jet Propulsion Laboratory, California Institute of Technology, JPL D-33509 Rev B, 2015.
- Louis, J. F.: A parametric model of vertical eddy fluxes in the atmosphere, *Boundary Layer Meteorol.*, 17, 187-202, 1979.
- McLay, J. G., Bishop, C. H., Reynolds, C. A.: Evaluation of the ensemble transform analysis perturbation scheme at NRL, *Mon. Wea. Rev.*, 136, 1093-1108, doi:10.1175/2007MWR2010.1, 2008,
- 10 McLay, J. G., Bishop, C. H., and Reynolds, C. A.: A local formulation of the ensemble transform (ET) analysis perturbation scheme, *Wea. Forecasting*, 25, 985-993, doi:10.1175/2010WAF2222359.1, 2010.
- Milewski, T., and Bourqui, M. S.: Assimilation of stratospheric temperature and ozone with an ensemble Kalman filter in a chemistry-climate model, *Mon. Wea. Rev.*, 139, 3389-3404, doi:10.1175/2011mwr3540.1, 2011.
- Peubey, C., and McNally, A. P.: Characterization of the impact of geostationary clear-sky radiances on wind analyses in a 4D-Var context, *Q. J. Roy. Meteor. Soc.*, 135, 1863-1876, doi:10.1002/qj.500, 2009.
- 15 Peuch, A., Thepaut, J. N., and Pailleux, J.: Dynamical impact of total-ozone observations in a four-dimensional variational assimilation, *Q. J. Roy. Meteor. Soc.*, 126, 1641-1659, doi:10.1002/qj.49712656605, 2000.
- Riishøjgaard, L. P.: On four-dimensional variational assimilation of ozone data in weather-prediction models, *Q. J. Roy. Meteor. Soc.*, 122, 1545-1571, doi:10.1002/qj.49712253505, 1996.
- 20 Rosmond, T. E.: A technical description of the NRL adjoint modeling system, NRL Publication NRL/MR/7532-97-7230, available at: <http://www.dtic.mil/docs/citations/ADA330960>, last access: 16 August 2017, Naval Research Laboratory, Monterey, California, USA, 57 pp., 1997.
- Rosmond, T., and Xu, L.: Development of NAVDAS-AR: non-linear formulation and outer loop tests, *Tellus*, 58A, 45-58, 2006.
- 25 Semane, N., Peuch, V. H., Pradier, S., Desroziers, G., El Amraoui, L., Brousseau, P., Massart, S., Chapnik, B., and Peuch, A.: On the extraction of wind information from the assimilation of ozone profiles in Meteo-France 4-D-Var operational NWP suite, *Atmos. Chem. Phys.*, 9, 4855-4867, doi:10.5194/acp-9-4855-2009, 2009.
- Xu, L., Rosmond, T., and Daley, R.: Development of NAVDAS-AR: formulation and initial tests of the linear problem, *Tellus*, 57A, 546-559, 2005.



Experiment Type	α	Ozone Observation Sampling	Ozone Error [%]	σ_{ob}	Radiance Observations	Radiance Error	Initial Conditions
<i>Sect. 4.1</i>							
Truth	0.5						Unperturbed
Ozone Only	0.5	global	0	0.1			Unperturbed
Ozone Only	0.5	global	0	0.1			Perturbed
<i>Sect. 4.2</i>							
Truth	0.0						Unperturbed
Truth	0.5						Unperturbed
Truth	1.0						Unperturbed
Baseline	0.0	global	0	0.1			Perturbed
Baseline	0.5	global	0	0.1			Perturbed
Baseline	1.0	global	0	0.1			Perturbed
Ozone Only	0.0	global	0	0.1			Perturbed
Ozone Only	0.5	global	0	0.1			Perturbed
Ozone Only	1.0	global	0	0.1			Perturbed
<i>Sect. 4.3</i>							
Ozone Only	0.0	global	0	0.1			Perturbed
Ozone Only	0.5	random	0	0.1			Perturbed
Ozone Only	0.5	polar-orbiting	0	0.1			Perturbed
<i>Sect. 4.4</i>							
Ozone Only	0.5	global	0	0.1			Perturbed
Ozone Only	0.5	polar-orbiting	2%	2%			Perturbed
Ozone Only	0.5	global	2%	2%			Perturbed
Ozone Only	0.5	global	5%	5%			Perturbed
Ozone Only	0.5	global	10%	20%			Perturbed
<i>Sect. 5.1</i>							
Baseline	0.5				All	Noisy	Perturbed
Baseline	0.5				All	Perfect	Unperturbed
<i>Sect. 5.2</i>							
Radiance & Ozone	0.5	global	0	0.1	All	Noisy	Perturbed
Radiance & Ozone	0.5	random	0	0.1	All	Noisy	Perturbed
Radiance & Ozone	0.5	polar-orbiting	0	0.1	All	Noisy	Perturbed
Radiance & Ozone	0.5	global	2%	2%	All	Noisy	Perturbed
Radiance & Ozone	0.5	random	2%	2%	All	Noisy	Perturbed
Radiance & Ozone	0.5	polar-orbiting	2%	2%	All	Noisy	Perturbed

Table 1. Experiment descriptions used in each subsection of this study. Columns indicate (1) experiment type, (2) covariance blending value, (3) ozone observation sampling, (4) ozone observation error, (5) background ozone error standard deviation, (6) radiance observations, (7) radiance error, and (8) initial conditions.



5

Fig. 1. Locations of ozone observations for (a) global, (b) random, and (c) polar-orbiting data. For global data these represent hourly coverage, while for polar and random data these are all the observations over a 24-hour period.

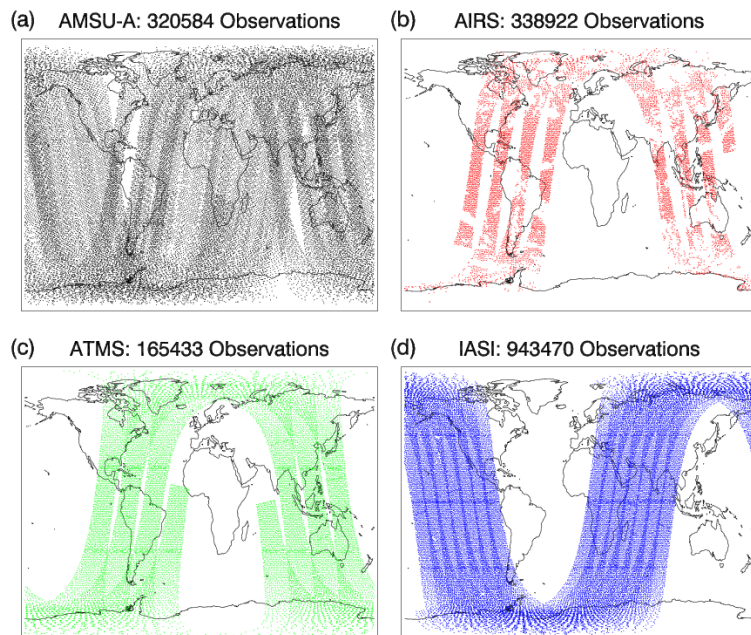


Fig. 2. Locations of simulated radiance observations for one 6-h update cycle centered at 06Z on 15 November 2014. Panels show observation locations for (a) AMSU-A, (b) AIRS, (c) ATMS, and (d) IASI.

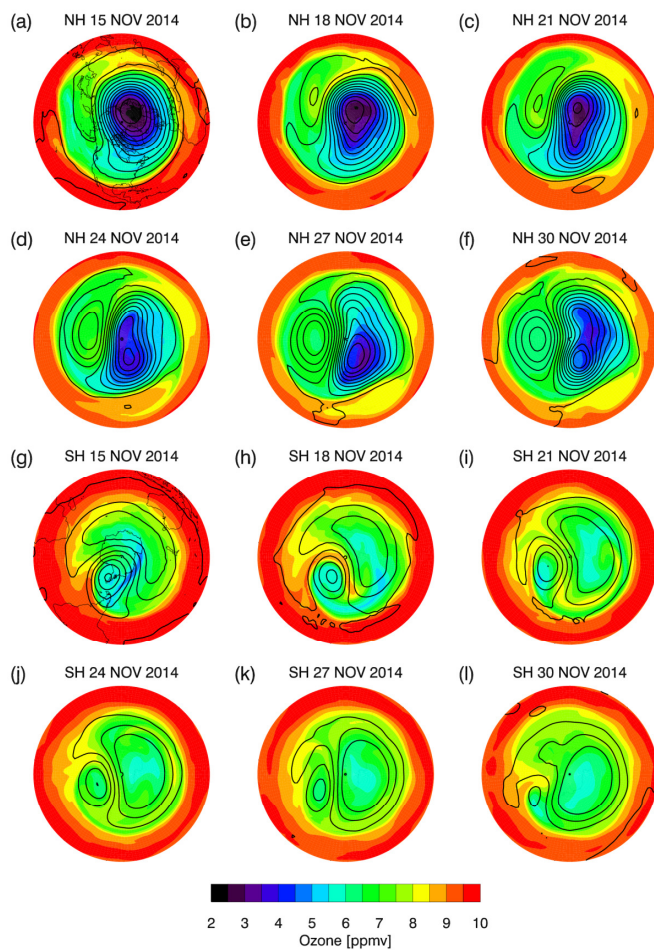


Fig. 3. Maps of ozone [ppbv] (colors) overlaid with geopotential height (black lines) at 200 m intervals for 15, 18, 21, 24, 27, and 30 November 2014. (a-f) are NH and (g-l) are SH. Red (blue) contours indicated high (low) ozone values. Continent lines are placed on the maps for 15 November.

5

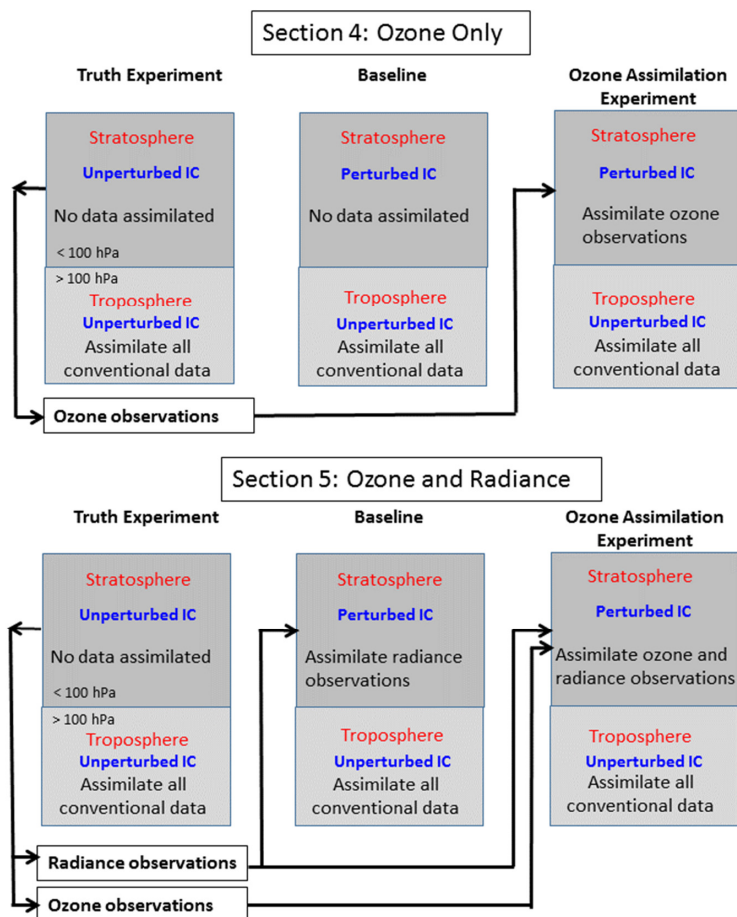


Fig. 4. Schematic diagram to illustrate the design for the experiments analyzed in Sect. 4 and Sect. 5. The truth experiment (TE) in both cases assimilates all conventional data in the troposphere (pressures > 100 hPa) and no data in the stratosphere (pressures < 100 hPa). In Sect. 4, the baseline experiment is the same as the TE, except for perturbed initial conditions (IC) in the stratosphere. The ozone assimilation experiment for Sect. 4 assimilates ozone observations created by the TE. In Sect. 5, the baseline includes assimilation of noisy radiance observations created from the TE. The ozone assimilation experiment in Sect. 5 includes both radiance and ozone observations from the TE.

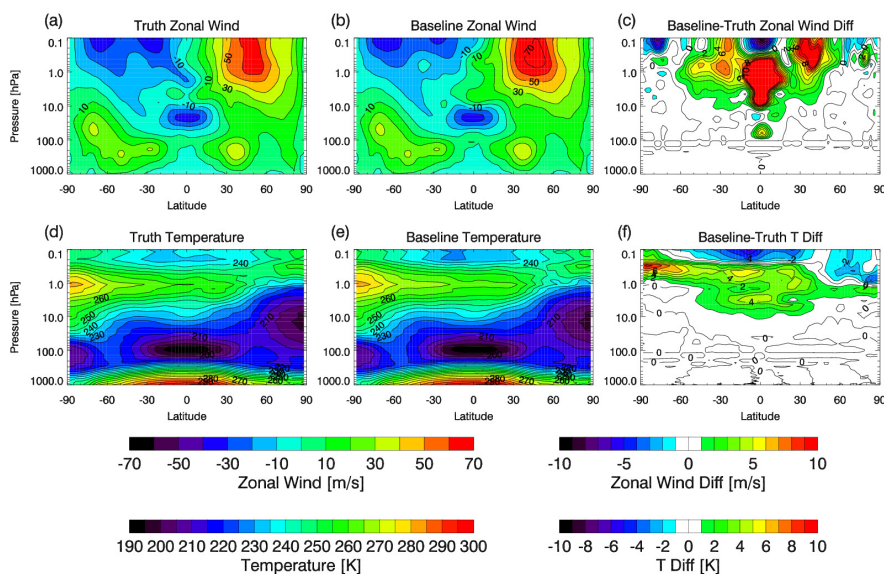


Fig. 5. Zonal mean zonal wind for the (a) truth experiment and (b) baseline experiments and (c) baseline-truth zonal wind difference. Zonal mean temperature for the (d) truth experiment and (e) baseline experiment and (f) baseline-truth temperature difference. Color bars are provided for zonal mean quantities and differences. Red (blue) indicates high (low) values for each quantity.

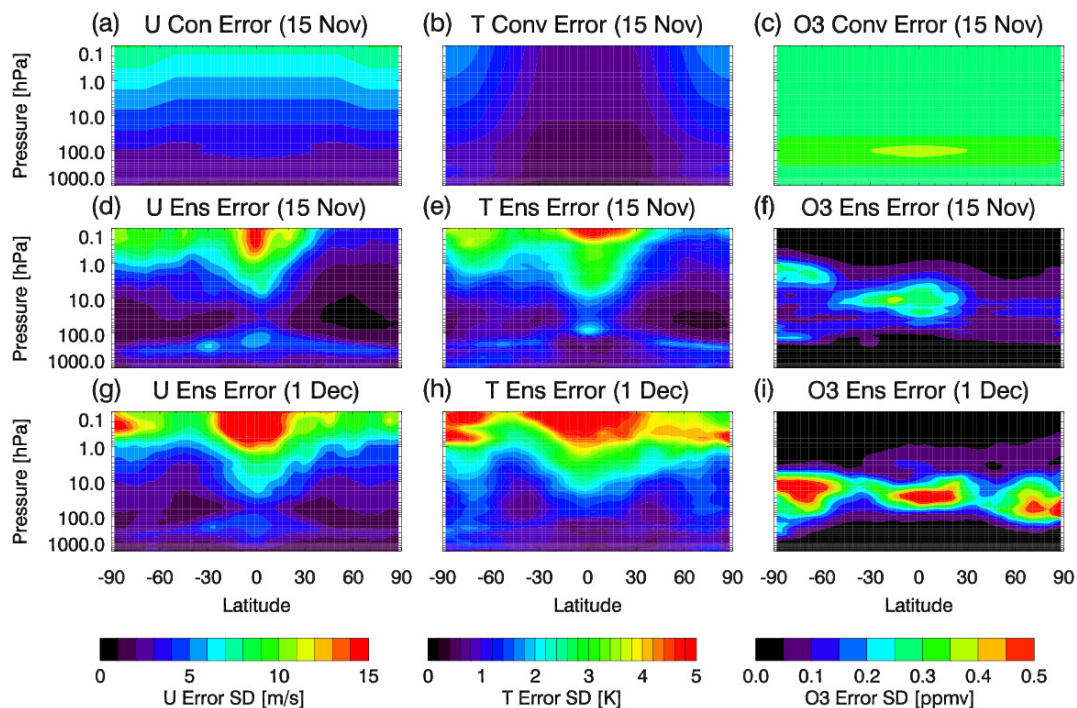


Fig. 6. Conventional background error standard deviations for (a) zonal wind, (b) temperature, and (c) ozone for 15 November 2014. Ensemble background error standard deviations for (d) zonal wind, (e) temperature, and (f) ozone for 15 November 2014. Ensemble background error standard deviations for (g) zonal wind, (h) temperature, and (i) ozone for 1 December 2014. Color bars are provided for zonal wind, temperature, and ozone, with red (blue) indicating high (low) values.

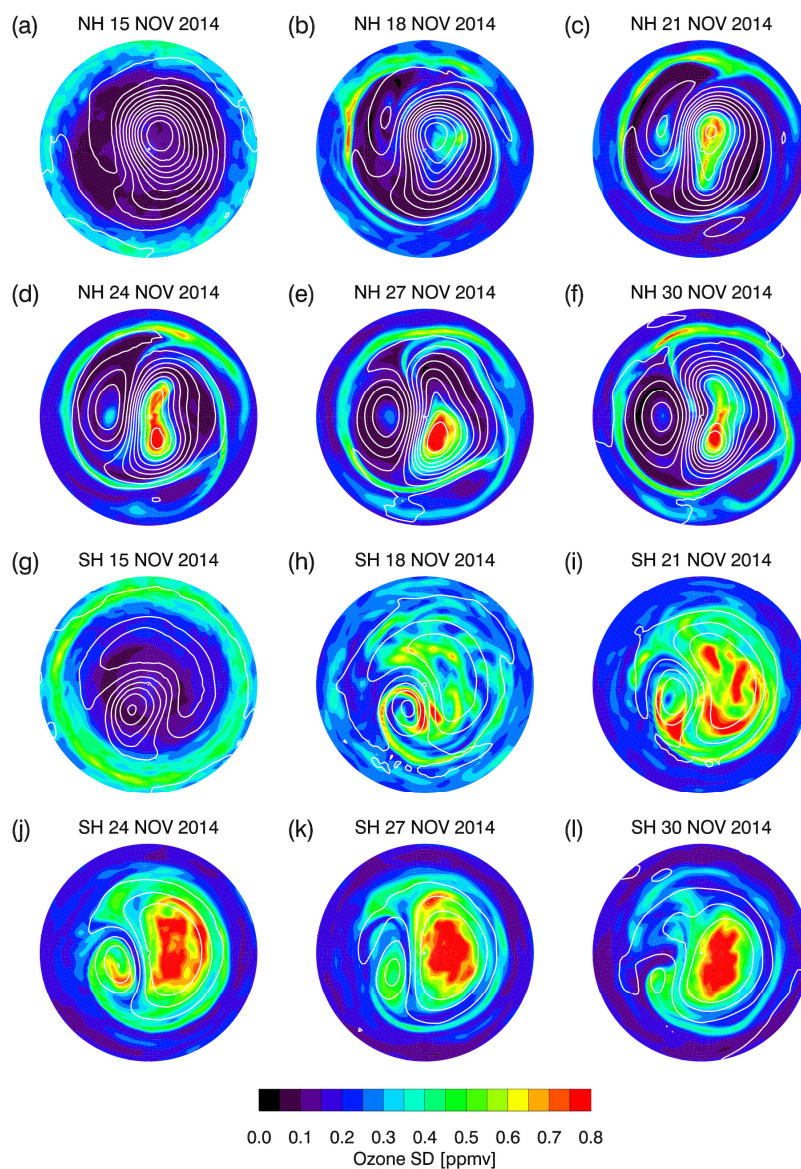


Fig. 7. Maps of ozone σ_{ens} [ppbv] (colors) overlaid with geopotential height (white lines) at 200 m intervals for 15, 18, 21, 24, 27, and 30 November 2014. (a-f) are NH and (g-l) are SH. Red (blue) contours indicated high (low) ozone values.

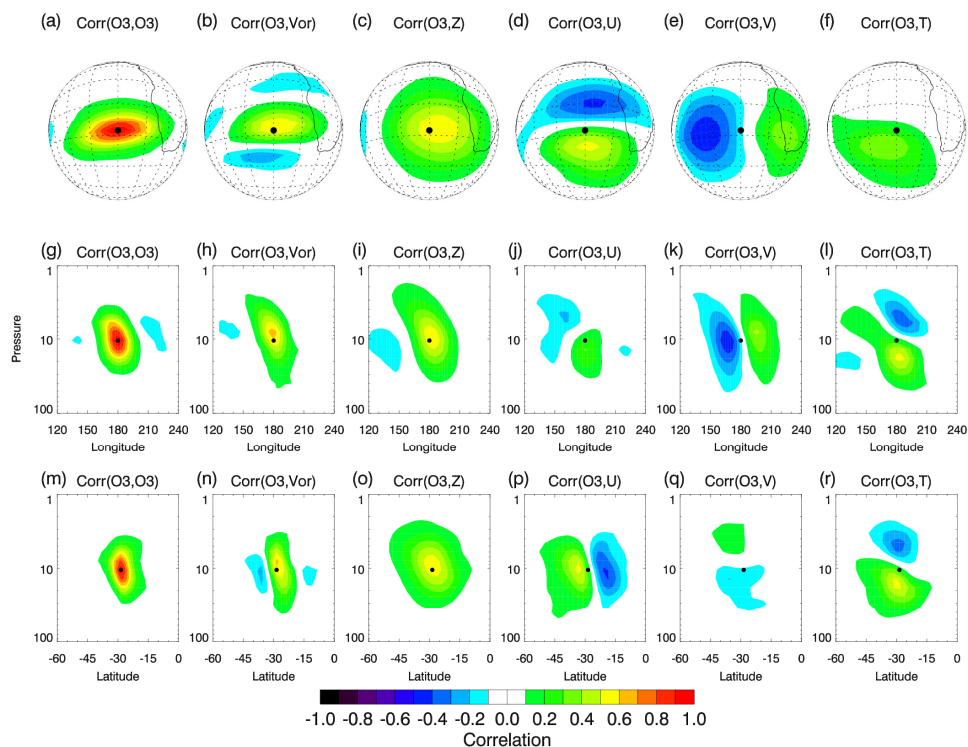


Fig. 8. Composite analysis of the ensemble cross-correlations between ozone and other variables on 30 November 2014. Calculation is an average at 10.5 hPa and latitude of 28.6°S, and the observation (black dot) is centered at 180° longitude (see text for details). Top row is the horizontal correlation using a satellite projection (grid lines at 10° spacing in longitude and latitude, and continental outline is seen for southern Africa), middle row is the longitude-pressure cross-section, and bottom row is the latitude-pressure cross-section. Columns indicate correlation between ozone and (1) ozone, (2) vorticity, (3) geopotential height, (4) zonal wind, (5) meridional wind, (6) temperature. Colors are correlation with red (blue) indicating high (low) values.

10

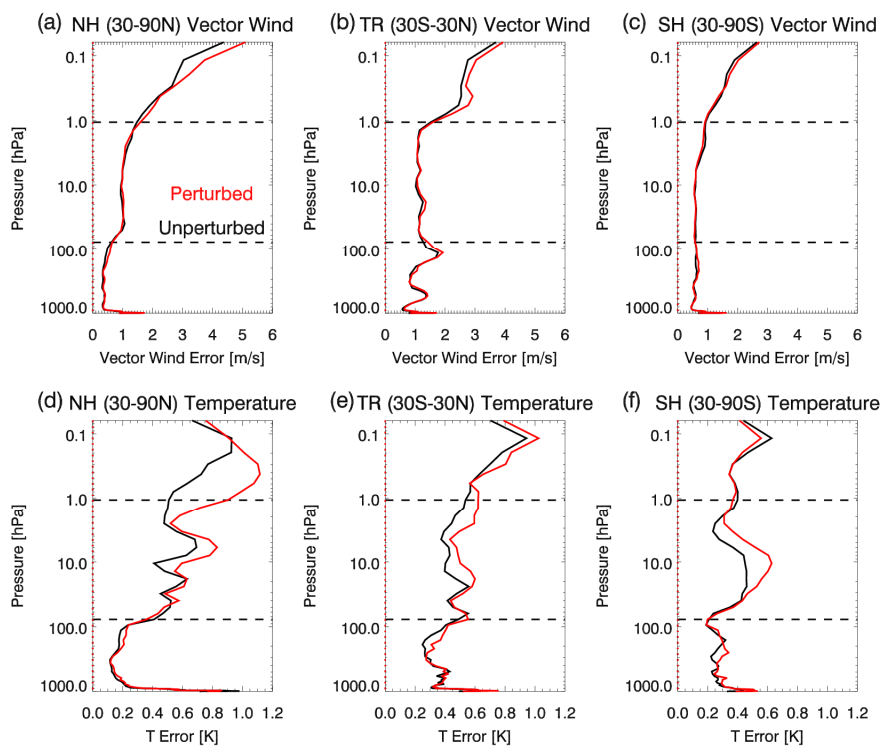


Fig. 9. RMS vector wind errors on 1 December 2014 for (a) NH, (b) TR, and (c) SH and RMS temperature errors for the (d) NH, (e) TR, and (f) SH. Black (red) lines are for experiments that assimilated perfect global ozone data with unperturbed (perturbed) initial conditions. Horizontal dashed lines indicate vertical range of assimilated stratospheric observations.

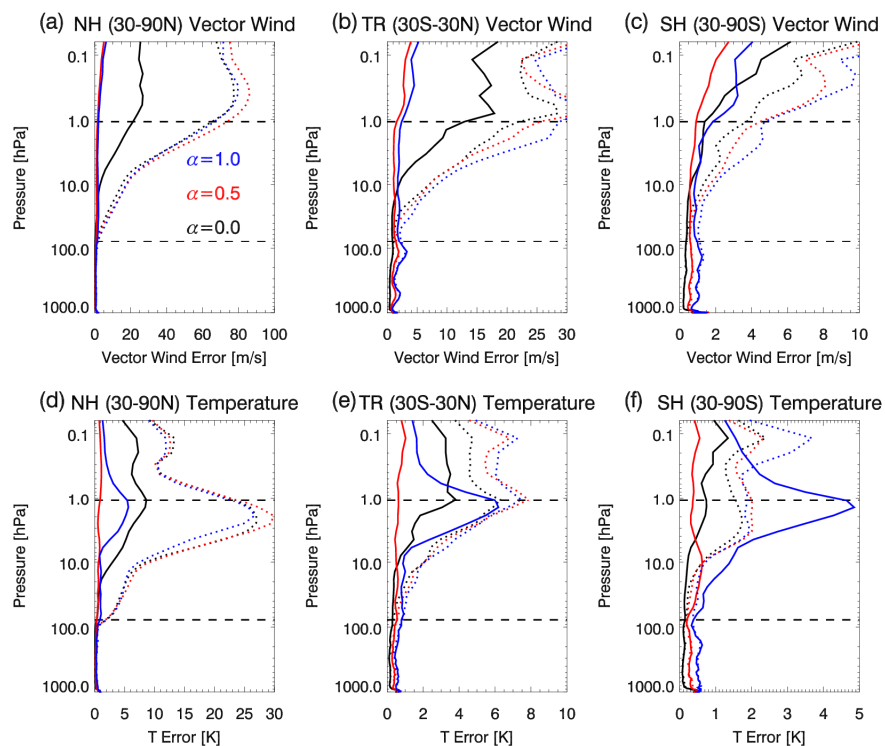


Fig. 10. RMS vector wind errors on 1 December 2014 for (a) NH, (b) TR, and (c) SH and RMS temperature errors for the (d) NH, (e) TR, and (f) SH. Solid (dotted) lines are for ozone assimilation experiments (baselines) with $\alpha = 0.0$ (black), 0.5 (red), and 1.0 (blue). Horizontal dashed lines indicate vertical range of assimilated stratospheric observations. Note that the ranges

5 of the horizontal axes for each panel varies based on maximum baseline errors.

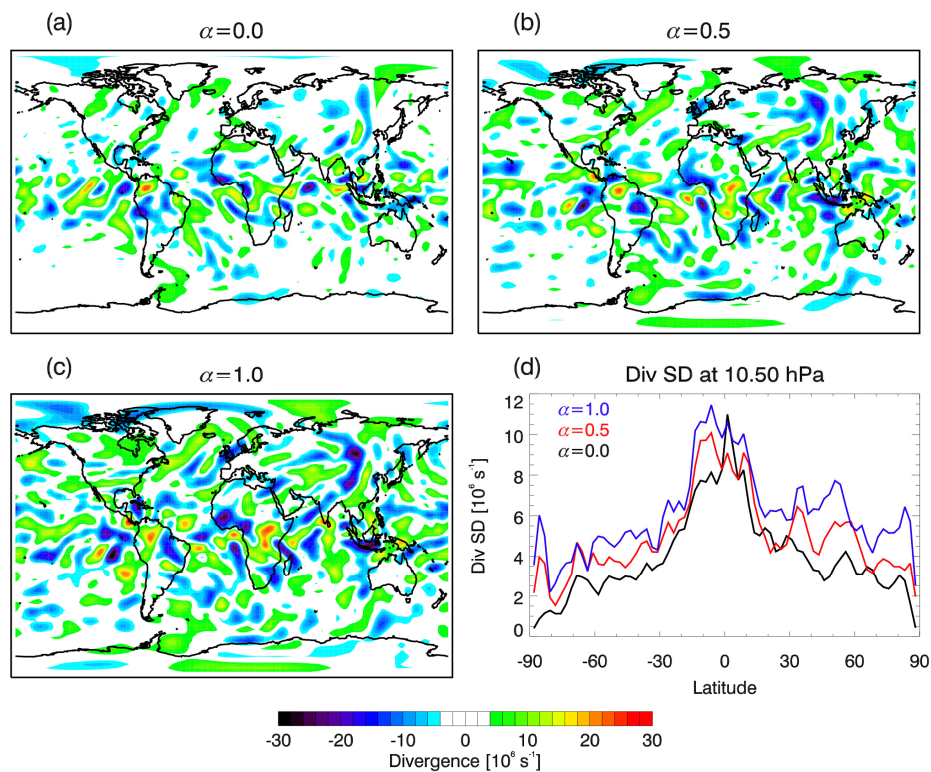


Fig. 11. Horizontal maps at 10.5 hPa of the divergence on 1 December 2014 for ozone assimilation experiments with (a) $\alpha = 0.0$, (b) $\alpha = 0.5$, and (c) $\alpha = 1.0$. Colors show divergence with red (blue) indicating high (low) values. (d) The standard deviation of the divergence as a function of latitude at 10.5 hPa. Lines are $\alpha = 0.0$ (black), $\alpha = 0.5$ (red), and $\alpha = 1.0$ (blue).

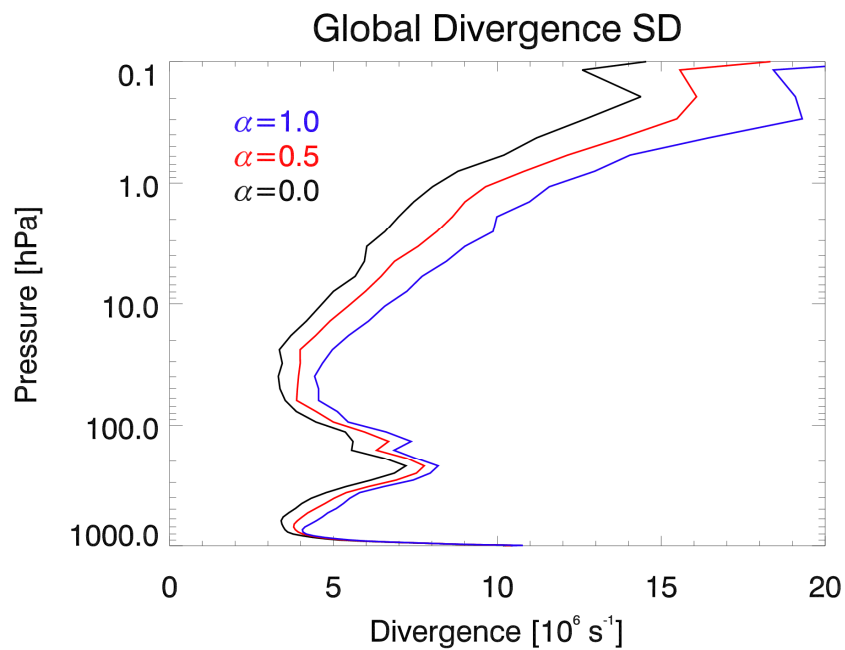


Fig. 12. Vertical profiles of the global standard deviation of the divergence for ozone assimilation experiments on 1 December 2014. Lines are $\alpha = 0.0$ (black), $\alpha = 0.5$ (red), and $\alpha = 1.0$ (blue).

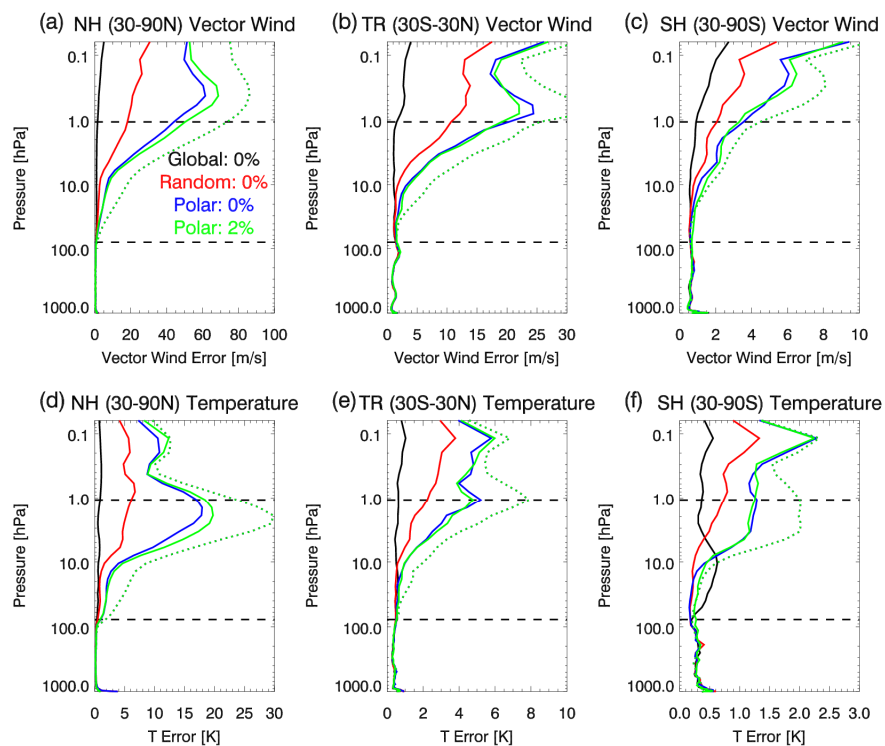


Fig. 13. RMS vector wind errors on 1 December 2014 for (a) NH, (b) TR, and (c) SH and RMS temperature errors for the (d) NH, (e) TR, and (f) SH. Solid (dotted) lines are for ozone assimilation experiments (baselines) for global: 0% error (black), random: 0% error (red), polar: 0% error (blue), and polar: 2% error (green). Horizontal dashed lines indicate vertical range of assimilated stratospheric observations. Note that the ranges of the horizontal axes for each panel varies based on maximum baseline errors.

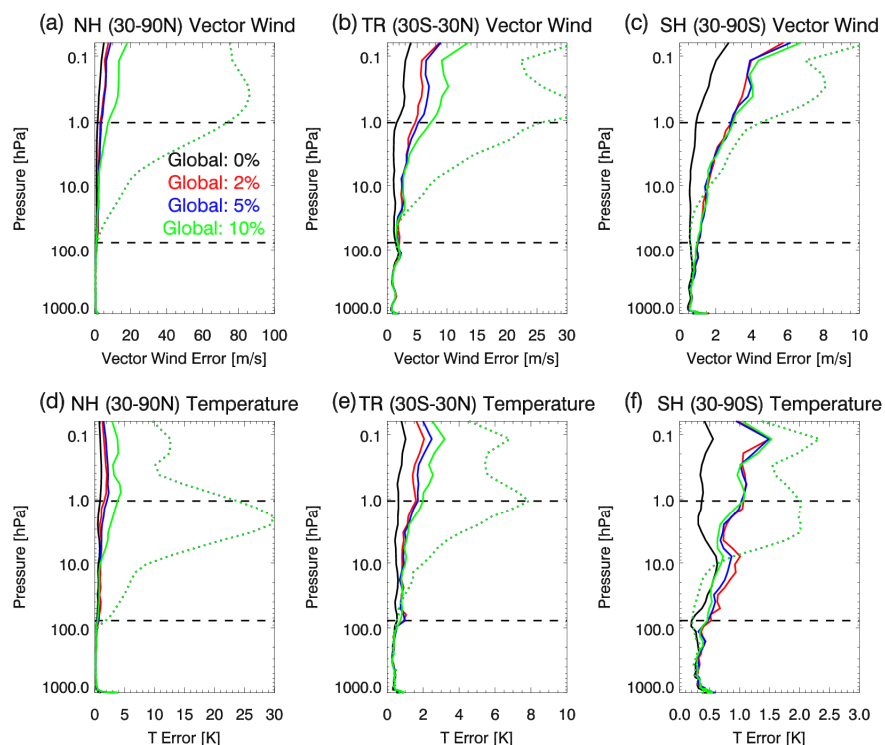


Fig. 14. RMS vector wind errors on 1 December 2014 for (a) NH, (b) TR, and (c) SH and RMS temperature errors for the (d) NH, (e) TR, and (f) SH. Solid (dotted) lines are for ozone assimilation experiments (baselines) for observation errors of 0% (black), 2% (red), 5% (blue), and 10% (green). Horizontal dashed lines indicate vertical range of assimilated stratospheric observations. Note that the ranges of the horizontal axes for each panel varies based on maximum baseline errors.

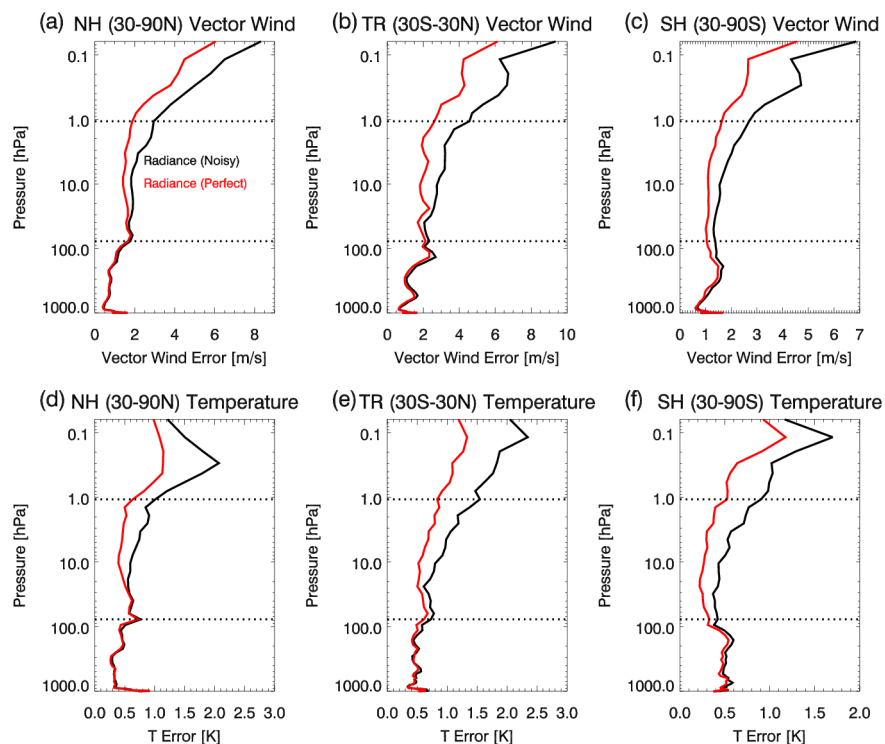


Fig. 15. RMS vector wind errors on 1 December 2014 for (a) NH, (b) TR, and (c) SH and RMS temperature errors for the (d) NH, (e) TR, and (f) SH. Black (red) lines are for assimilation of noisy (perfect) radiance data. Horizontal dashed lines indicate
5 vertical range of assimilated stratospheric observations. Note that the ranges of the horizontal axes for each panel varies based on maximum errors.

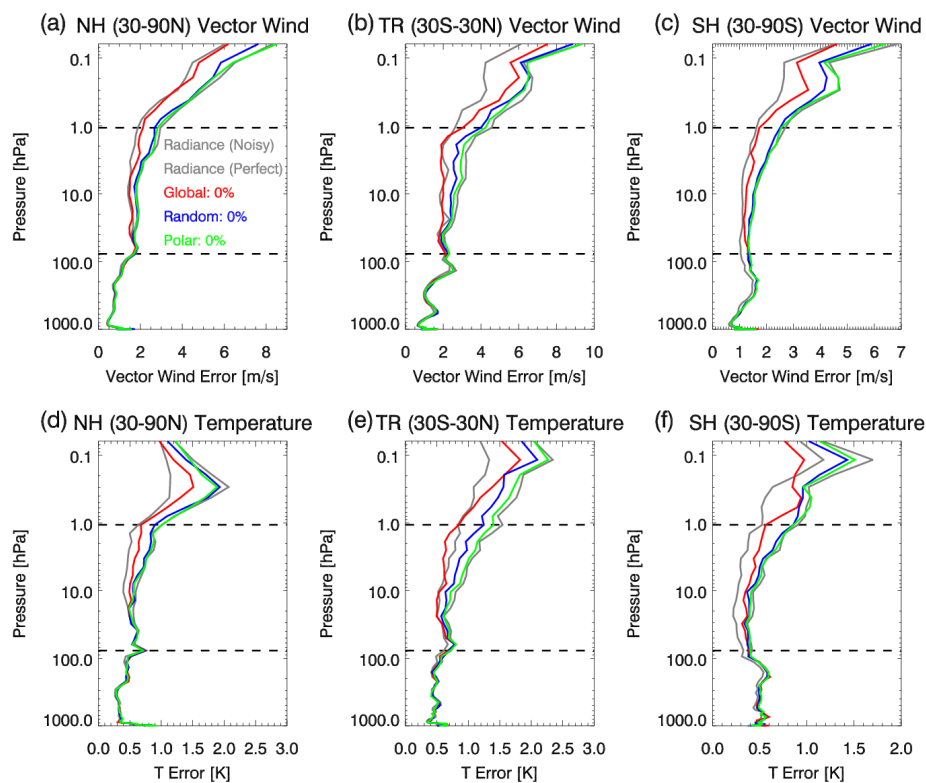


Fig. 16. RMS vector wind errors on 1 December 2014 for (a) NH, (b) TR, and (c) SH and RMS temperature errors for the (d) NH, (e) TR, and (f) SH. Colored lines are for ozone assimilation experiments with noisy radiance and perfect ozone data using sampling pattern of global (red), random (blue), and polar (green). Grey lines are for radiance only assimilation for noisy and perfect data (same as in Fig. 15). Horizontal dashed lines indicate vertical range of assimilated stratospheric observations. Note that the ranges of the horizontal axes for each panel varies based on maximum errors.

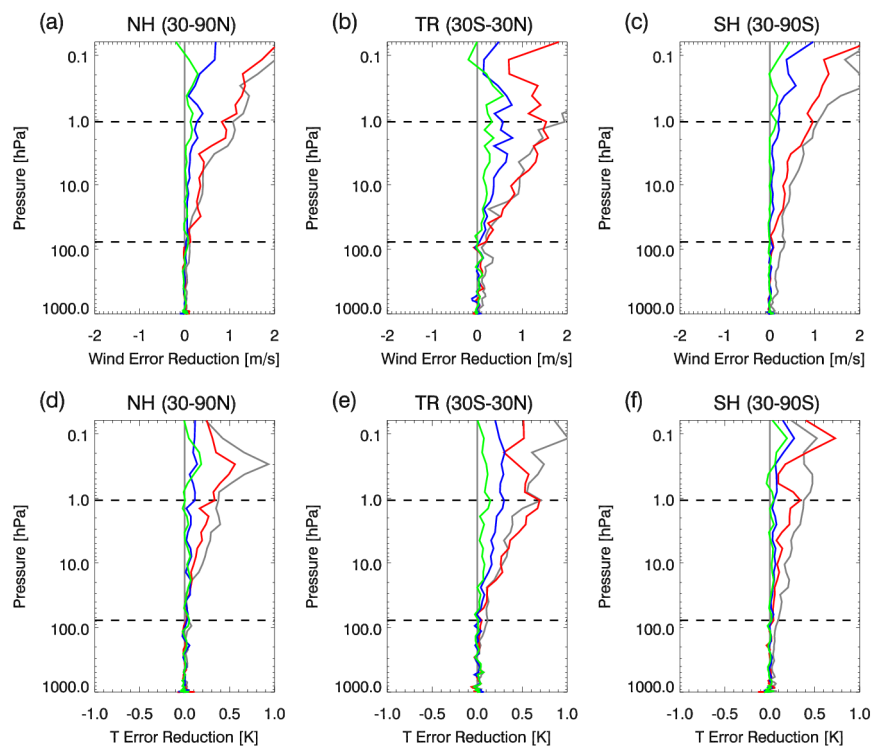


Fig. 17. RMS vector wind error differences (with respect to assimilation of radiance only) on 1 December 2014 for (a) NH, (b) TR, and (c) SH and RMS temperature error differences for the (d) NH, (e) TR, and (f) SH. Lines are for ozone assimilation experiments with perfect ozone data and sampling pattern of global (red), random (blue), and polar (green). Grey line indicates results for assimilation of perfect radiances. Horizontal dashed lines indicate vertical range of assimilated stratospheric observations.

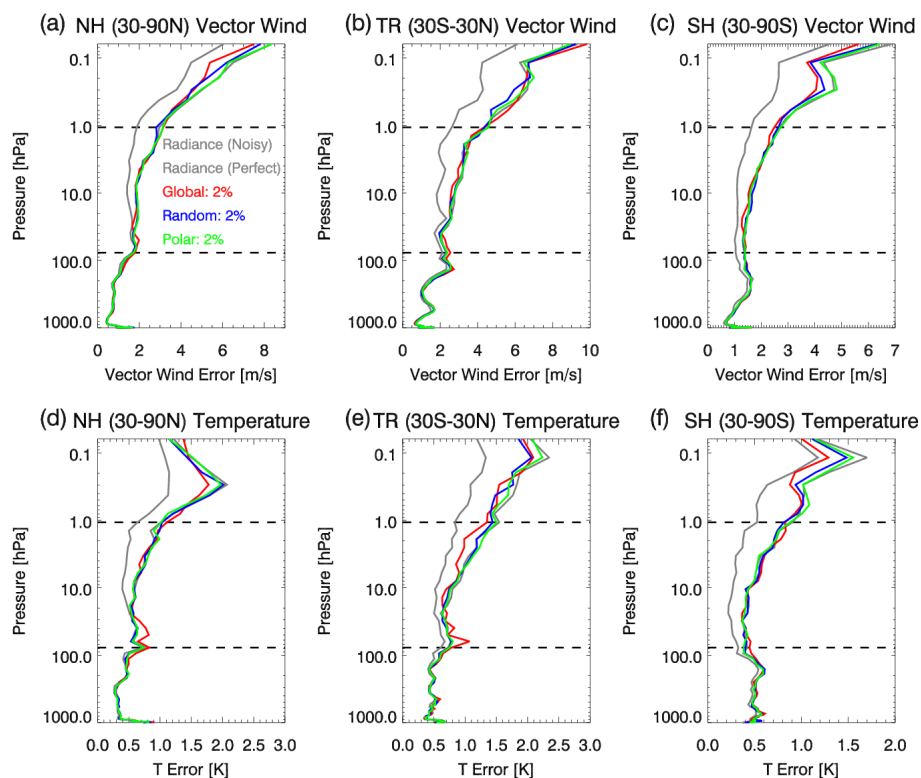


Fig. 18. RMS vector wind errors on 1 December 2014 for (a) NH, (b) TR, and (c) SH and RMS temperature errors for the (d) NH, (e) TR, and (f) SH. Colored lines are for ozone assimilation experiments with noisy radiance and ozone data with 2% error using sampling pattern of global (red), random (blue), and polar (green). Grey lines are for radiance only assimilation for noisy and perfect data (same as in Fig. 15). Note that the ranges of the horizontal axes for each panel varies based on maximum errors. Horizontal dashed lines indicate vertical range of assimilated stratospheric observations.

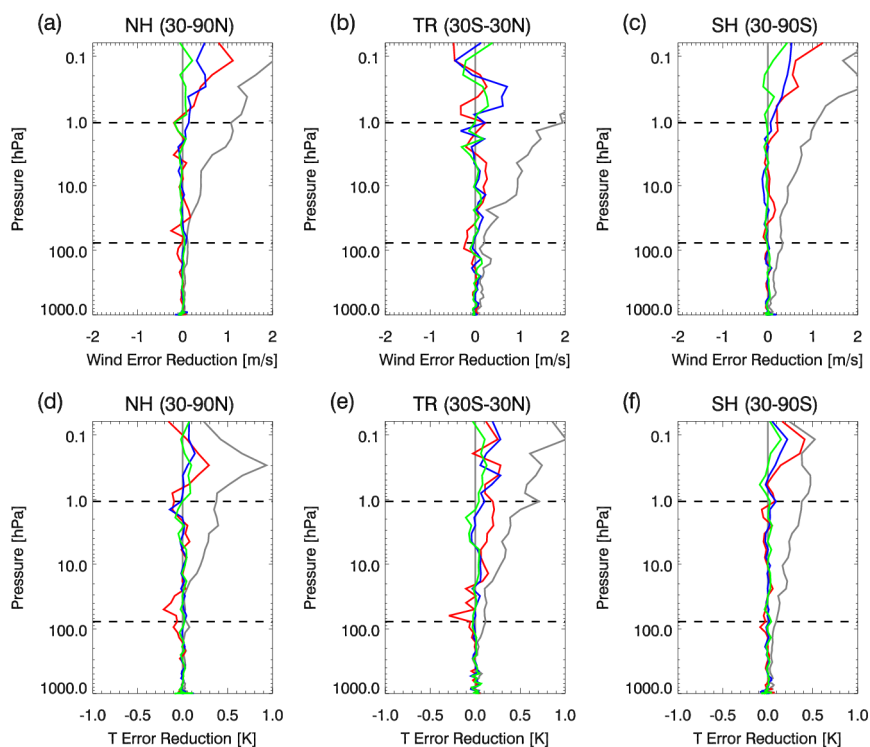


Fig. 19. RMS vector wind error differences (with respect to assimilation of radiances only) on 1 December 2014 for (a) NH, (b) TR, and (c) SH and RMS temperature error differences for the (d) NH, (e) TR, and (f) SH. Lines are for ozone assimilation experiments with ozone data that has imposed errors (2%) and sampling pattern of global (red), random (blue), and polar (green). Grey line indicates results for assimilation of perfect radiances. Horizontal dashed lines indicate vertical range of assimilated stratospheric observations.